

# **Study on the optimization of a slotted hydrofoil using Genetic algorithm**

Mahya Hajihassanpour and Alireza Khodabaksh

## **Abstract**

In this study, a hydrofoil is slotted to passively control the cavitating flow features. Here, we would like to investigate the effect of the slot location and the slot angle on the cavity size and the lift coefficient as well. For this aim, preconditioned Euler equations are considered as the governing equations. The Frink numerical method is developed here to discretize the spatial terms in these equations. So that controlling the artificial oscillations and for stability reasons, an artificial dissipation term with an appropriate sensor is utilized. The numerical method is validated by the simulation of the sheet and mid-chord cavitation flows over NACA 66 (MOD). Then, a multi-objective optimization is done to find a slotted NACA 66 (MOD) hydrofoil with objective functions, which are maximization of the lift coefficient and minimization of the total length of the cavity. For constructing an optimizer, a surrogated model based on the kriging metamodel and the genetic algorithm are used. Initial sample points are obtained using the Latin Hypercube algorithm. The outcome of the optimization process is an optimized slotted NACA 66 (MOD) hydrofoil satisfying the cost functions defined. In addition, different maps including a variation of the total length of the cavity, the length of the leading-edge and mid-chord cavities created by the slot, and the lift coefficient with respect to the slot location and the slot angle are obtained. These maps show how the cavity size and lift coefficient will be affected by changing the slot location and the slot angle and they are useful for designing purposes. Indications are that while using the slot can favorably reduce the total length of the cavity, it will also undesirably reduce the lift coefficient.

## **Keywords**

Slotted hydrofoil, Cavitation, Optimization, Genetic algorithm, Surrogate model, Frink numerical method

## **1. Introduction**

Cavitating flows are widely seen in many practical applications, for instance, they occur in pumps, pipes, hydro turbines, and blood vessels, or on the watercraft including ships, boats, amphibious, submarines, and hovercraft. The Cavitation will take place when the liquid is accelerated and consequently the local pressure becomes lower than the vapor pressure. In such a condition, the preexisting vapor nucleus will grow in the liquid medium and eventually create a cavity pocket filled with both liquid and many vapor nucleus. When these nuclei arrive at places with higher pressures, condensation occurs. In the condensation process, the nucleus violently collapses and high-pressure waves will be generated that cause erosion, annoying sounds, and vibration that may cause a shorter lifetime for the product and affect its performance. The flow control techniques can be used to avoid these unfavorable things. Different cavitation types have been explored in nature, for instance, sheet cavitation, vortex cavitation, and cloud cavitation [1], and they have been widely investigated, however, less attention has been made to controlling this type of flows. Flow control techniques can be categorized into passive and active methods, and both of them have been previously used for controlling cavitating flows. In the case of active flow control, different methods such as the injection [2-5] or suction [6] are used to control the cavitation flows. The passive flow control methods because of the advantages of simplicity and economic efficiency in comparison with the active flow control methods, are more applied to real applications. Different passive control methods have been utilized for controlling cavitating flows, for example, vortex generators [7, 8], leading-edge slats [9], leading-edge serration [10], slotted hydrofoils [11-15], micro-cylinders [16], hydrofoils with cavity [17], Roughness [18], and flexible hydrofoil [19].

A few studies about the slotted hydrofoil have been performed in the literature [11-15]. Note that, in the literature [13, 14], the work of Qun et al. [9] has been mentioned as the origin of the slotted hydrofoil used for the cavitation control, however, we think it is a slatted hydrofoil which is basically different from the slotted hydrofoil, and the idea of using slotted hydrofoils comes from the work of Capurso et al. [11]. Capurso et al. [11, 12] have proposed a passive control system consisting of three slots located near the leading-edge of the NACA 0009 hydrofoil. Their results show a 93% reduction for the total length of the cavity, but a 25% reduction in the lift coefficient. The optimization has not been performed by them.

Conesa and Liem [13, 14] have studied the effect of the entry and exit widths of the slot and its angle on the performance of the Clark-Y hydrofoil, but they have fixed the slot location near the leading-edge in the optimization process. Their study shows that the optimized slotted hydrofoil can achieve higher performance with a 50% reduction in cavity pocket in comparison with the base hydrofoil.

An experimental and numerical study has been done by Ni et al. [15] to investigate the performance of a slotted hydrofoil operating close to a free surface. The slotted hydrofoil is constructed from the base hydrofoil NACA 634-021. No optimization has been performed, and the slotted hydrofoil had a better performance in comparison with the base hydrofoil.

Here, the sheet cavitation is focused on checking the effectiveness of the use of a slot for controlling cavitating flows over a hydrofoil. In addition, NACA 66 (MOD) is served as the base hydrofoil because of its wide usage in many products.

Physics of the cavitating flows can be investigated by considering inviscid, laminar, and turbulent fluid flow depending on the fluid flow conditions. By assuming water as the main medium, the Reynolds number is often high in real applications so that the laminar cavitating flow can be only seen seldom, however, the inviscid flow condition can provide acceptable results. The pressure distribution over the hydrofoil determines the cavity pocket size and the lift coefficient, and they can reasonably be captured by the solution of Euler equations. In inviscid flow simulation, a fewer number of grid points in comparison with turbulent flows are required in simulations and then the computational cost can dramatically be decreased.

The system of equations governing the cavitating flows has to be solved using an appropriate numerical method. Different methods have been utilized in the literature for solving these governing equations, such as the central finite difference [20], compact [21], central finite volume [22], Quadratic Upstream Interpolation for the Convective Kinematics (QUICK) [23], weighted essentially non-oscillating (WENO) [24], immersed boundary [25], upstream finite element [26], and discontinuous Galerkin [27, 28] methods. Here, the Frink numerical method [29] is applied to discretize the governing equation, and an appropriate artificial dissipation term, based on the one proposed by Jameson et al. [30], is added for suppressing artificial oscillations in the solution domain and to provide a stable and accurate solution. By this method, we are able to simulate cavitating flows with reasonable accuracy and computational time.

Nowadays, designing an engineering artifact usually requires to solve a complicated optimization problem often involving multiple objectives. The solution to these complex design optimization problems, such as the problem that is addressed in this paper, are generally computationally expensive. In order to reduce the computational costs metamodel approximations are intensively used in the literature [31, 32]. Metamodels use limited combinations of inputs (sample points) and outputs to provide a mapping from the input space to the output space which essentially reduces the computational cost [33, 34].

Metamodels are used in a wide variety of applications and come in several forms. Metamodels can be either deterministic or stochastic, low-order or high-order polynomial regression models, discrete or continuous, and local or global. Some of the better-known metamodels are the Multivariate Adaptive Regression Splines, Radial Basis Function, Polynomial Regression, Neural Networks, Kriging, etc. [31]. The advantages or disadvantages of metamodels vary case by case and we cannot easily say essentially one of them is better than the others, and an extensive study is needed between metamodels to judge their priority, which is beyond the scope of the paper.

In this paper, a Kriging metamodel is used. Kriging metamodel is a global, continuous, deterministic, and high-order regressional model [34]. Developed originally in geostatistics, which is later used in many engineering disciplines [35]. The Kriging interpolation not only generates a metamodel, but it also estimates the uncertainty of the generated output. The Kriging method is essentially a maximum likelihood estimator. Like any other maximum likelihood estimators, Kriging is also facing difficulties as the correlation matrix becomes singular if the sample points are not chosen appropriately. Thus, Choosing the sample data points is of paramount importance to have a Kriging metamodel that both represents the design space adequately and does not encounter any numerical difficulties. Usually to determine the sample points the theory of the Design of Experiments (DoE) is employed. Several used DoE methods are the factorial, central decomposition, alphabetical optimal, and Box-Behnken methods [36, 37]. These methods usually tend to push the sample points towards the boundaries of the design space. More recent methods address this problem and try to uniformly distribute the sample points within the boundaries. To name a few, Maximum Entropy, MiniMax, Orthogonal Arrays, and Latin Hypercube algorithms can be mentioned [31, 32, 36]. Latin Hypercube Sampling (LHS) is a straightforward well-

established sampling method in the literature that is chosen to be used in this research. In LHS an even random sampling is employed and then all the chosen variables are randomly combined to give the samples required.

While the metamodels together with DoE methods are used to find out the optimization functions defined in the design space, the optimizers are required to figure out where minimums occur. The optimizers can be categorized into two gradient-based and gradient-free groups [38]. As the name suggests, a gradient-based optimizer uses the gradient of the objective function to find the optimum solution. This dependence on the gradient raises two main issues. First, to use a gradient-based optimizer the gradient of the function must be either known analytically or computed numerically. This increases the computational cost. Second, and more importantly, a gradient-based optimizer can get stuck in a local optimum. On the other hand, a gradient-free/heuristic/Metaheuristics optimizer uses a random operator to search the design space. Decades of research resulted in the development of many Metaheuristics. To name a few well-known metaheuristics, we may mention Particle Swarm Optimization (PSO), Differential Evolution (DE), Genetic Algorithms (GA), and Ant Colony Optimization (ACO) [39]. Inspired by Darwin's natural evolution theory, the GA mimics the natural evolution to find the optimal solution [38, 40]. Within the GA, the design parameters are interpreted as characteristics of individuals. Taking all individuals among a population, the solutions evolve through cross-over, mutation, and elitism operators to find the optimum.

The random operator helps the Genetic Algorithm to explore the design space better and the gradient-independence empowers it to deal with any kind of objective function. This rigorous searching capability grants the metaheuristics and the GA particularly the name "global optimization methods". Nevertheless, the exploration capability comes at a cost. The GA usually requires more function evaluations than gradient-based optimizers to converge. This usually makes it difficult to use the metaheuristics for computationally expensive problems [38].

## 2. Governing equations

Steady inviscid cavitating fluid flows are governed by preconditioned Euler equations with exploiting the artificial compressibility method can be written as follows:

$$\boldsymbol{\Pi} \frac{\partial \mathbf{Q}}{\partial \tau} + \frac{\partial \mathbf{F}}{\partial x} + \frac{\partial \mathbf{G}}{\partial y} - \mathbf{S}_c = 0 \quad (1)$$

where  $\boldsymbol{\Pi}$  indicates the preconditioning matrix which is

$$\boldsymbol{\Pi} = \begin{bmatrix} \frac{1}{\rho_m \beta^2} & 0 & 0 & 0 \\ 0 & \rho_m & 0 & u \Delta \rho_l \\ 0 & 0 & \rho_m & v \Delta \rho_l \\ \frac{\alpha_l}{\rho_m \beta^2} & 0 & 0 & 1 \end{bmatrix} \quad (2)$$

The artificial time is denoted by  $\tau$  and derivatives with respect to this variable should go to zero for satisfying the consistency and convergence conditions. This means that this formulation can be used only for steady-state solutions. This is corresponding with the physics we are dealing with because we are going to optimize a hydrofoil experiencing quasi-steady sheet cavitation flow. The cavitation source term  $\mathbf{S}_c$  plays an important rule in cavitation modeling and it is defined in a way to appropriately model the mass transfer between the liquid and vapor phases that occurred in the cavitation process. We will further discuss this term in the next section. The flux vectors  $\mathbf{H} = (\mathbf{F}, \mathbf{G})$  and the solution vector  $\mathbf{Q}$  are written as follows:

$$\mathbf{Q} = \begin{bmatrix} p \\ u \\ v \\ \alpha_l \end{bmatrix}, \quad \mathbf{F} = \begin{bmatrix} u \\ \rho_m u^2 + p \\ \rho_m u v \\ \alpha_l u \end{bmatrix}, \quad \mathbf{G} = \begin{bmatrix} v \\ \rho_m u v \\ \rho_m v^2 + p \\ \alpha_l v \end{bmatrix} \quad (3)$$

The solution vector is consist of the pressure  $p$ , the velocity vector  $(u, v)$ , and the liquid volume fraction  $\alpha_l$ . The subscripts  $l$ ,  $v$ , and  $m$  are added to facilitate identifying the liquid, vapor, and mixture states. While the liquid density  $\rho_l$  and  $\rho_v$  are supposed to be constant, the mixture density is allowed to vary according to the relation  $\rho_m = \alpha_l \rho_l + \alpha_v \rho_v$ . Note that the summation of volume fraction of different phases is always unity, i.e.,  $\alpha_l + \alpha_v = 1$ . Moreover,  $\rho_l = 1$  and  $\rho_v = 0.01$  are

used here that prove to be suitable values for simulating cavitating flows in a water medium. In Eq. (2), the density jump is indicated by  $\Delta\rho_l = \rho_l - \rho_v$ .

Following the concept of the artificial compressibility method, the artificial compressibility coefficient denoted by  $\beta$  is used in the governing equations to tackle the pressure-velocity coupling problem pertaining to incompressible flows. It is a user-defined parameter and here we simply use a constant value  $\beta = 3$  similar to [27, 41].

## 2.1. Cavitation modeling

As mentioned in the previous section, the cavitation process is modeled by the cavitation source term  $S_c$  which is

$$S_c = \begin{bmatrix} (\dot{m}^+ + \dot{m}^-) \left(1 - \frac{1}{\rho_v}\right) \\ 0 \\ 0 \\ \dot{m}^+ + \dot{m}^- \end{bmatrix} \quad (4)$$

where  $\dot{m}^-$  models the evaporation phenomena which is the mass transfer from the liquid to the vapor phase, and it is vice versa for  $\dot{m}^+$  which represents the condensation process wherein the vapor phase transits to the liquid phase. These two variables are differently defined in the literature [42-46]. Here, the relations proposed by Merkel et al. [42] is exploited, i.e.,

$$\begin{aligned} \dot{m}^+ &= \left(\frac{C_{prod}}{t_\infty}\right) (1 - \alpha_l) \text{Max}(0, p - p_v) \\ \dot{m}^- &= \left(\frac{C_{dest}}{t_\infty}\right) \frac{1}{\rho_v} \alpha_l \text{Min}(0, p - p_v) \end{aligned} \quad (5)$$

These relations have been proposed by Merkel et al. [42] that derived from their experimental work. Numerical studies [27, 47] show that these relations are reliable and accurate for simulating cavitating flows. The parameters  $C_{prod}/t_\infty$  and  $C_{dest}/t_\infty$  are the constant parameters which control the liquid production and destruction rates, respectively. They are user-defined parameters where  $C_{prod}/t_\infty = 1$  and  $C_{dest}/t_\infty = 80$  are used here. Numerical studies done in literature [27, 47] prove these values lead to accurate numerical results. Finally, the vapor pressure  $p_v$  is obtained according to the predefined cavitation number  $\sigma = 2(p_\infty - p_v)$  where  $p_\infty$  is the pressure far enough from the hydrofoil surface which is assumed unit. Note that all the variables used in the present study are non-dimensional identical to the ones presented in [27].

### 3. Numerical method

#### 3.1. Spatial discretization

So that being able to simulate cavitating flows, we should suitably address the solution of the governing equation (1) by means of a numerical method. Here, the Frink numerical method is used to discretize the spatial derivative terms in the governing equations.

By integrating Eq. (1) through the surface A of an element, it can be rewritten as

$$\int_A \left[ \boldsymbol{\Pi} \frac{\partial \mathbf{Q}}{\partial \tau} + \frac{\partial(\mathbf{F})}{\partial x} + \frac{\partial(\mathbf{G})}{\partial y} - \mathbf{S}_c \right] dA = 0 \quad (6)$$

In the finite volume method variables are assumed to be constant through an element, then

$$\int_A \boldsymbol{\Pi} \frac{\partial \mathbf{Q}}{\partial \tau} dA = \boldsymbol{\Pi} \frac{\partial \mathbf{Q}}{\partial \tau} A \quad (7)$$

For the spatial derivative of inviscid fluxes, we have

$$\int_A \left[ \frac{\partial \mathbf{F}}{\partial x} + \frac{\partial \mathbf{G}}{\partial y} \right] dA = \int_A [\nabla \cdot \mathbf{H}] dA \quad (8)$$

and then using the divergence theorem applied to triangular domain results in

$$\int_A [\nabla \cdot \mathbf{H}] dA = \oint_{\partial A} [\mathbf{H}^* \cdot \hat{\mathbf{n}}] dL = \sum_{k=1}^{N_{faces}=3} (\mathbf{H}^* \cdot \hat{\mathbf{n}})_k L_k \quad (9)$$

where  $\mathbf{H}_k^*$  is the numerical flux for the  $k$ -th face of the element, and it depends on the flux vectors in two neighboring elements sharing that face. After finding the flux vectors in two neighboring elements by exploiting the Frink numerical method, the Lax numerical flux method is used to calculate the numerical flux. The calculation of the Lax numerical flux method will be explained later. Variable  $\hat{\mathbf{n}}$  is the normal outward vector. The face length of the triangle element is denoted by  $L$ .

The integration of the cavitation source term  $\mathbf{S}_c$  can be written as

$$\int_{\mathbf{A}} \mathbf{S}_c \, d\mathbf{A} = \mathbf{S}_c \, \mathbf{A} \quad (10)$$

The integration of the artificial dissipation terms should be carefully evaluated and it will be addressed in the next section. Finally, the discretization process, by substituting Eqs. (7)-(10) into (6), results in

$$\frac{\partial \mathbf{Q}}{\partial \tau} = \frac{\boldsymbol{\Pi}^{-1}}{A} \left[ \mathbf{S}_c \, \mathbf{A} - \sum_{k=1}^{N_{faces}} (\mathbf{H}^* \cdot \hat{\mathbf{n}})_k L_k \right] = \mathbf{R} \quad (11)$$

where  $\mathbf{R}$  is called the right-hand side vector.

### 3.1.1. The Frink numerical method

The higher-order finite volume methods can be derived using reconstructing fluxes at the element faces. To show how the Frink numerical method can be used to increase the order of accuracy of the solution from the first-order in the classical finite volume method to the second-order one, refer to Fig. 1. While in the classical first-order finite volume methods variables at the faces can be read as  $q_{f_1} = q_{f_2} = q_{f_3} = q_c$ , in the Frink numerical method [29], they are reconstructed as follows:

$$\begin{aligned} q_{f_1} &= q_c + \frac{1}{3} \left[ \frac{1}{2} (q_{n_1} + q_{n_2}) - q_{n_3} \right] \\ q_{f_2} &= q_c + \frac{1}{3} \left[ \frac{1}{2} (q_{n_2} + q_{n_3}) - q_{n_1} \right] \\ q_{f_3} &= q_c + \frac{1}{3} \left[ \frac{1}{2} (q_{n_1} + q_{n_3}) - q_{n_2} \right] \end{aligned} \quad (12)$$

The remaining variables to be defined are the nodal values denoted by  $q_{n_1}$ ,  $q_{n_2}$ , and  $q_{n_3}$ . An area-weighted average, among the elements sharing the node, is used to calculate values in nodes.

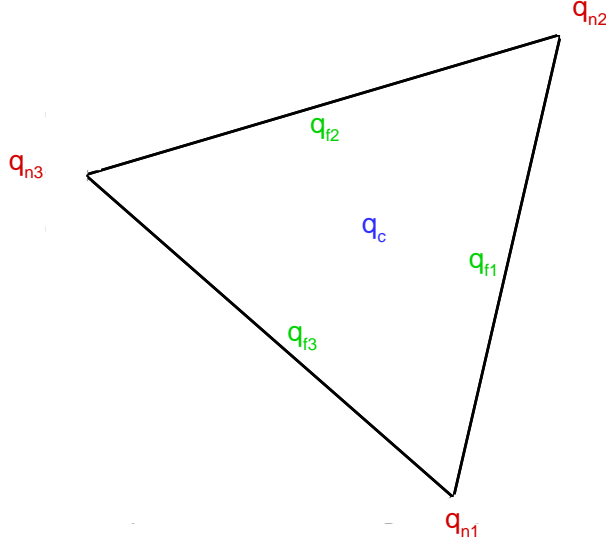


Fig. 1 Nomenclatures used for constructing fluxes in the Frink numerical method.

### 3.1.2. Numerical flux

The Lax numerical flux is used here to address the Riemann problem for the jumps between two neighboring elements. If the flux in a face is denoted by the subscript  $L$  and its neighbor's value by  $R$ , then

$$H_k^* = \frac{1}{2} (H_L + H_R - C\lambda\Pi(Q_R - Q_L)) \quad (13)$$

where  $\lambda$  is the largest eigenvalue of the system of equations

$$\lambda = \sqrt{u_L^2 + v_L^2} + \sqrt{u_L^2 + v_L^2 + \beta^2} \quad (14)$$

and  $C$  is a constant parameter with  $C \leq 1$  for satisfying stability conditions. Selecting higher values for  $C$  means adding more dissipation to the solution domain that may cause reducing global accuracy. Here,  $C = 0.25$  is used to consequently provides accuracy and stability needs.

### 3.1.3. Artificial dissipation

Although discretization has been done, we should care about the artificial non-physical oscillations that occur near the cavity zone which could make the solution unstable. To prevent such undesirable oscillations in the solution, the artificial dissipation term  $\mathbf{D}$  [30] is added to the right-hand side of Eq. (11) as follows:

$$\frac{\partial \mathbf{Q}}{\partial \tau} = \mathbf{R} + \mathbf{D} = \mathbf{R}' \quad (15)$$

The artificial dissipation for the  $j$ -th element can be written as:

$$\mathbf{D}_j = \sum_{k=1}^{N_{faces}=3} \mathbf{d}_{j_k} \quad (16)$$

where  $k$  indicates the face number. If the solution vector in neighbor element through the  $k$ -th face is shown by  $\mathbf{Q}_j^k$ , then the dissipation term can be written as follows:

$$\mathbf{d}_{j_k} = -\left(\frac{A_j}{\Delta \tau} + \frac{A_j^k}{\Delta \tau}\right) \left[ \frac{\varepsilon_{j_k}}{2} (\mathbf{Q}_j - \mathbf{Q}_j^k) \right] \quad (17)$$

where  $\Delta \tau$  is the artificial time step. The artificial viscosity coefficient  $\varepsilon$  has to be determined such that tends to zero where the solution is smooth and to a definite value in non-smooth regions which normally occur near the cavity zone which is the origin of the artifact oscillations generated due to the sharp jump in the density variable across the interface of the two phases. In order to determine the artificial viscosity coefficient, we follow the idea presented in Jameson et al. work [30] which is:

$$\begin{aligned} \varepsilon_{j_k} &= \kappa_\rho \gamma_{j_k} \\ \gamma_{j_k} &= \left| \frac{\rho_j - \rho_j^k}{\rho_j + \rho_j^k} \right| \end{aligned} \quad (18)$$

and  $\kappa_\rho = 0.025$  is chosen here.

### 3.2. Temporal discretization

The Euler method is used here for discretizing the temporal derivative in Eq. (15)

$$\frac{Q^{m+1} - Q^m}{\Delta \tau} = \mathbf{R}'^m \quad (19)$$

where superscript  $m$  indicates the time-level.

## 4. Optimization procedure

Firstly, the number of optimization parameters or constraints should be determined. Those are the slot angle and the slot location with considered limitations here as  $0^\circ \leq \theta \leq 85^\circ$  and  $0 \leq x_{slot} \leq 0.4$ , respectively. The optimization parameters are geometrically introduced in Fig. 2. As shown in this figure, the slot location varies from the middle chord up to about the leading-edge and its angle is defined clockwise. Afterward, the Latin Hypercube Sampling method (LHS) with an affine mapping is used in order to generate initial sampling points  $N_{LHS}$  in the design space. Here, initial sampling points are supposed to be 40 points. Then, the CFD simulations are performed for the given sampling points to calculate the lift coefficient and the total length of the cavity appeared on the hydrofoil that called the objective functions. The lift coefficient function is represented by  $C_l = f(x_{slot}, \theta)$  and the total length of cavity is denoted by  $L_c = g(x_{slot}, \theta)$  will be found using Gaussian Process Regression or Kriging method which is exploited to construct the surrogate model. The lift coefficient can be calculated using the integral of the pressure in the direction perpendicular to the far-field flow divided by  $0.5\rho u_\infty^2$ . In the case of the total length of the cavity  $L_c$ , it will be calculated using the following relation

$$L_c = L_{c_1} + L_{c_2} \quad (20)$$

where  $L_{c_1}$  denotes the length of the leading-edge cavity and  $L_{c_2}$  is the length of the mid-chord cavity. The leading-edge cavity is a cavity formed on the front hydrofoil, and the mid-chord cavity is a cavity that appeared on the rear hydrofoil created by slotting the original hydrofoil. The length of the leading-edge/mid-chord cavity is the horizontal distance between two points where the pressure over the hydrofoil becomes lower than the vapor pressure and where it becomes higher than the vapor pressure.

These objective functions will be served as an input to a genetic algorithm (GA) to result in an accurate and fast optimization scheme. The Pareto front comes out from GA and the final design point will be selected from the set of points on the Pareto front. These operations will be repeated  $N_{GA}$ -th times. In each iteration, the new design points will be added to the older ones, i.e.,  $N_{LHS}$  will be updated. Subsequently, CFD simulations, Kriging, and GA as well will be carried on. Here,  $N_{GA}$  equals to 5 which means that five generations are considered in the genetic algorithm. The number of new design points will not be greater than 20 in each iteration, and if not, 20 points will be selected randomly. The latter is presumed to reduce the computational cost. This optimization procedure/algorithm is illustrated in Fig. 3.

This optimization procedure is performed in Matlab. The information of the sampling points or the new design points will be automatically transformed into a meshing tool which is Gambit here to generate the mesh for the CFD tool. The CFD tool is also a homemade code using the Frick method as a discretization algorithm and C++ as a programming language.

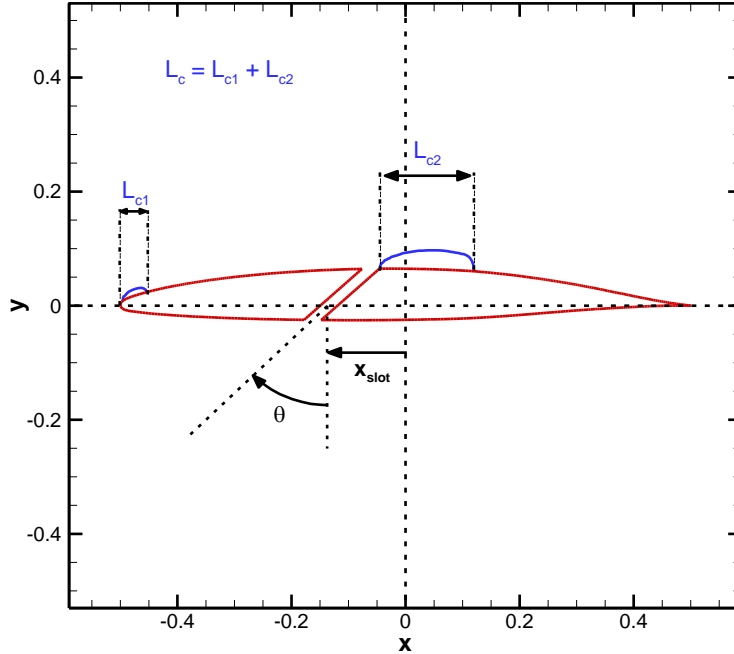


Fig. 2 Nomenclatures related to the optimization parameters, the total length of the cavity, the length of the leading-edge cavity, and the length of the mid-chord cavity.

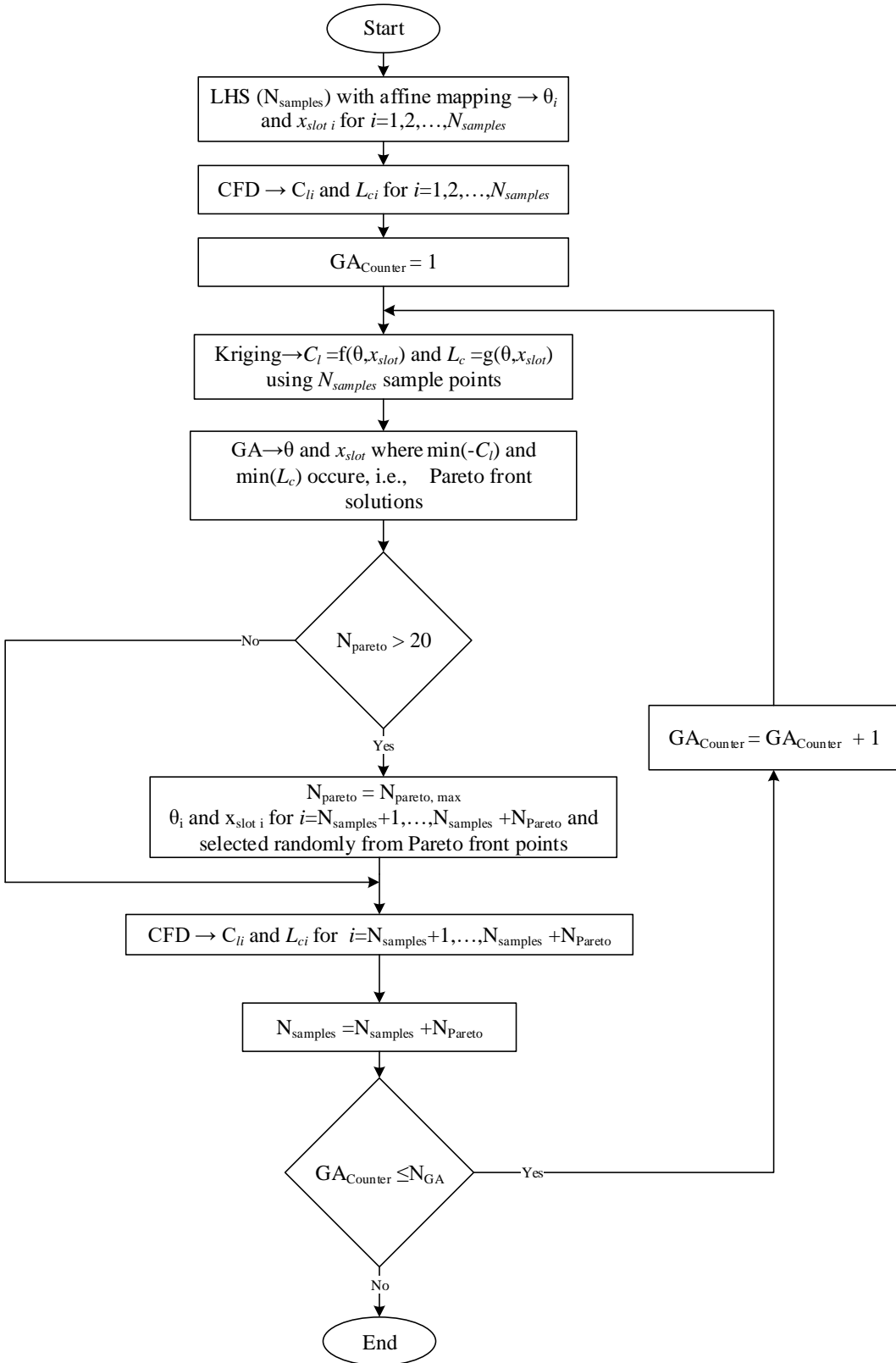


Fig. 3 Flowchart describing the optimization process.

## 5. Results

In this section, the numerical results are presented. The numerical method is first evaluated in subsection 5.1 wherein the sheet/leading-edge and mid-chord cavitations have been simulated and are compared with the experimental data. After proving that the numerical method works fine, then the results for the slotted hydrofoil and its optimized shape will be discussed.

### 5.1. Validation

Once the original hydrofoil NACA 66(MOD) is slotted, instead of one cavity pocket over the original hydrofoil surface, two-cavity pockets might form over the modified hydrofoil. The first cavity pocket over the modified hydrofoil can be seen as a sheet/leading-edge cavity, and the second one is similar to the mid-chord cavity over the original hydrofoil. Thus, the sheet and mid-chord cavitation phenomenon are simulated here to show that the numerical method arranged here can be effectively used for the optimization of the slotted hydrofoil. The sheet cavitation will be created over the original hydrofoil when water flows over NACA 66 (MOD) at the angle of attack  $\alpha = 4^\circ$  and cavitation number  $\sigma = 0.84$ , and by considering  $\alpha = 1^\circ$  and  $\sigma = 0.43$  the mid-chord cavitation will be formed.

In Fig. 4, the generated grid with 16330 triangle elements is shown. The grid type is chosen to be triangular because they can be used over arbitrary and complex geometries such as the one we are dealing with in this paper, i.e., slotted hydrofoil. Moreover, they are suitably work in inviscid flows, because there is no need for having high-resolution grids close to the walls due to the presence of the boundary layer. As can be seen in Fig. 4, the radius of the far-field boundary is assumed ten times of the hydrofoil chord. Moreover, a finer grid is used close to the hydrofoil surface while a coarser grid is used far from its surface. Using high-resolution grids near the hydrofoil will help to sharply capture the cavity pocket, and a coarse grid near the far-field boundary will aid to damp the artificial incoming and outgoing waves occurred there.

In Fig. 5, the numerical results for the simulation of the sheet cavitation over the original NACA 66 (MOD) hydrofoil are illustrated. The density, pressure, and velocity magnitude contours

indicate that the cavitation phenomenon can be expected over the suction side of the hydrofoil wherein the velocity magnitude is increased and subsequently the pressure is decreased to a lower value than the vapor pressure. Moreover, the velocity magnitude immediately reduces when the cavity pocket is closed which is a sign for the re-entrant jet. In Fig. 5(d), the calculated surface pressure coefficient by the present numerical method is compared with the experimental data [48]. As can be seen in this figure, the agreement between numerical results is satisfactory. The pressure in the cavity pocket remains unchangeable that excellently follows experimental pieces of evidence. In addition, the pressure recovery at the trailing edge is captured by the present numerical method efficiently.

In Fig. 7, the numerical results by utilizing the Frink numerical method are shown and compared with the experimental data [48]. Here, the mid-chord cavitation occurs. It means that the cavitation is not started from the leading-edge. Instead, it is started in the middle of the suction side and this is the reason it is called the mid-chord cavitation. As indicated in this figure, the numerical results obey the expected physical behaviors and also agrees with the experimental data.

From the obtained numerical results for the simulation of these two cavitation types, it can be concluded that the numerical framework set up here can be used to effectively simulate different quasi-steady cavitation flows encountered in the present study. After validating the CFD, we are now ready to pay attention to the optimized slotted hydrofoil in the next section.

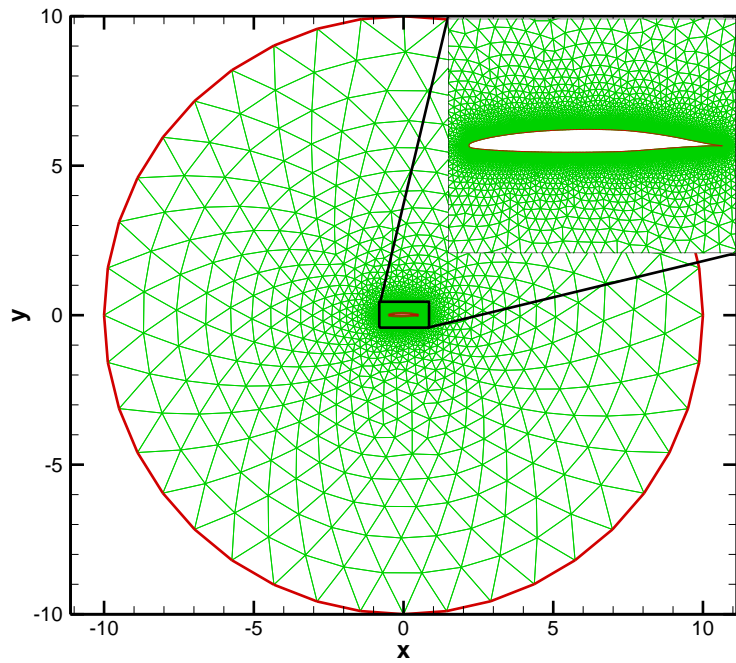
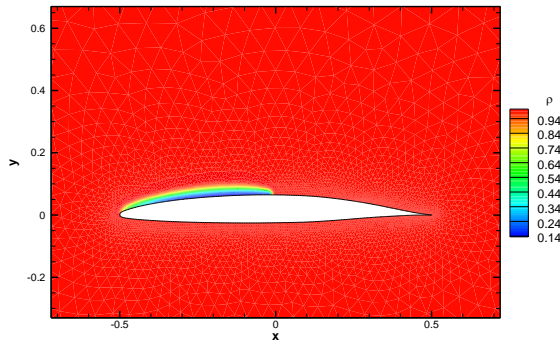
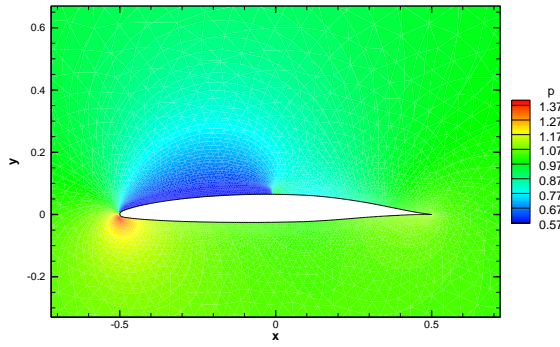


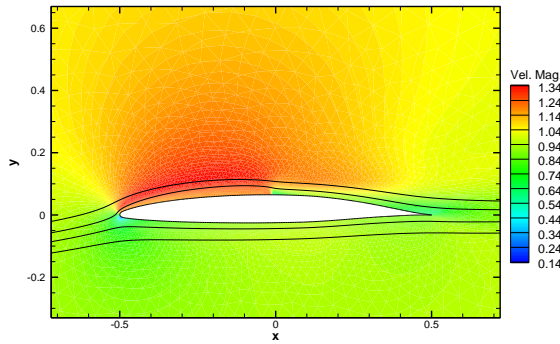
Fig. 4 Generated grid for the original NACA 66 (MOD) hydrofoil.



(a)



(b)



(c)

Fig. 5 Contours of a) the density, b) the pressure, and c) the velocity magnitude with the streamlines computed by the Frink numerical method for the problem of cavitating flow over NACA 66 (MOD) at  $\sigma = 0.84$  and  $\alpha = 4^\circ$ .

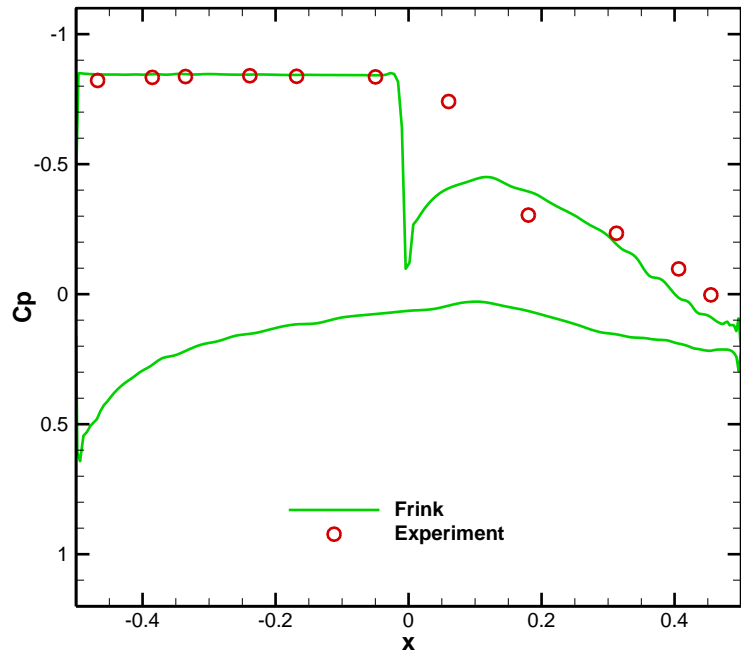
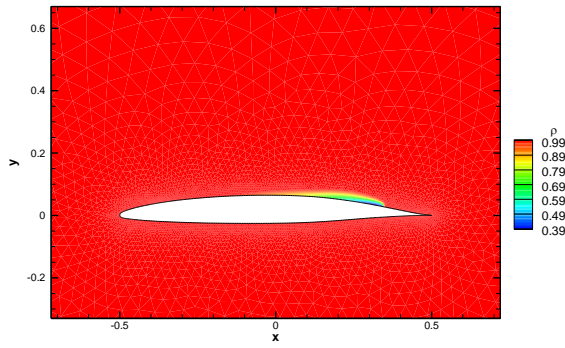
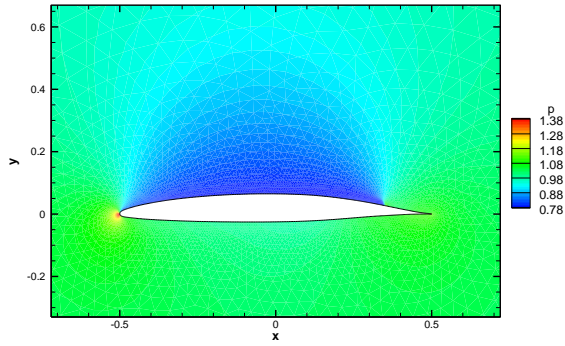


Fig. 6 Comparison of the pressure coefficient obtained by the Frink numerical method and experimental data[48] for the problem of cavitating flow over NACA 66 (MOD) at  $\sigma = 0.84$  and

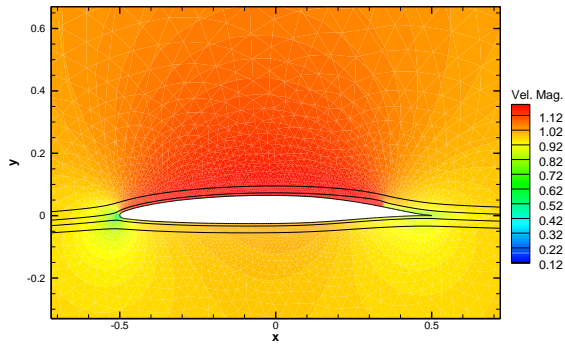
$$\alpha = 4^\circ.$$



(a)



(b)



(c)

Fig. 7 Contours of a) the density, b) the pressure, and c) the velocity magnitude with the streamlines computed by the Frink numerical method for the problem of cavitating flow over NACA 66 (MOD) at  $\sigma = 0.43$  and  $\alpha = 1^\circ$ .

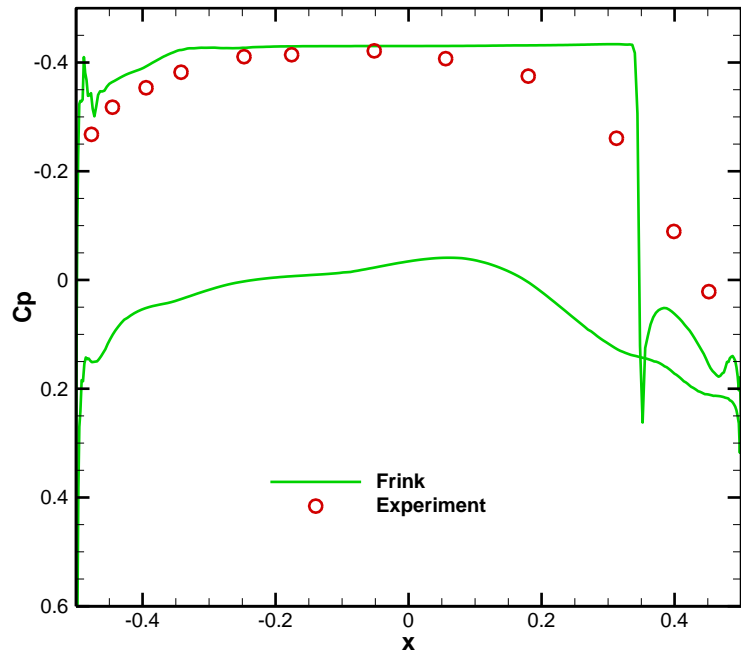


Fig. 8 Comparison of the pressure coefficient obtained by the Frink numerical method and experimental data[48] for the problem of cavitating flow over NACA 66 (MOD) at  $\sigma = 0.43$  and

$$\alpha = 1^\circ.$$

## 5.2. Optimization of slotted hydrofoil

The goal of this study is to optimize the slotted NACA 66 (MOD) hydrofoil immersed in water at cavitation number  $\sigma = 0.84$  and angle of attack  $\alpha = 4^\circ$ . As discussed in detail in the optimization procedure, 40 initial sampling points are used to train the optimizer. These initial sampling points are obtained by employing the Latin Hypercube Sampling, and these points are depicted in Fig. 9(a). By advancing in the optimization procedure, new design points will be added to assess the objective functions and to find the optimum points. All the points used in the optimization process are illustrated in Fig. 9(b) and it can be seen that many new points are inserted in the upper right side of the figure where the slots are created close to the leading-edge with higher angles. It means that the optimizer seeks the optimal point there, and by adding many new points in that region, it improves the high-fidelity model.

The output of the optimization will be the objective functions as a function of the optimization parameters, i.e.,  $C_l = f(x_{slot}, \theta)$  and  $L_c = g(x_{slot}, \theta)$ . These objective functions can be constructed using any surrogated models such as the regression or fitting methods. Here a fitting method is used to reconstruct the objective functions when the optimization process has been ended.

In Fig. 10, the contours related to  $L_{c_1}$  and  $L_{c_2}$  are shown. From Fig. 10(a) it can be concluded that generally at a given slot location the leading-edge cavity will reach its minimum size around  $\theta = 45^\circ$ , while lower and higher angles than this angle will cause having larger leading-edge cavity size. At a given slot angle, moving the slot location from the middle to the leading-edge will favorably result in decreasing in  $L_{c_1}$ . Thus, smaller  $L_{c_1}$  will be found around  $\theta = 45^\circ$  and high slot angles.

In the case of  $L_{c_2}$ , as depicted in Fig. 10(b), at a given slot location the mid-chord cavity will reach its maximum size around  $\theta = 60^\circ$ , while lower and higher angles than this angle will cause having larger leading-edge cavity size. At a given slot angle, by increasing the slot location,  $L_{c_2}$  will

disadvantageously increase. Thus, for having smaller  $L_{c_2}$ , higher slot angles should be used with a slot placed around the middle.

The contours of the objective functions  $C_l$  and  $L_c$  are illustrated in Fig. 11 and it is obvious that the objective functions are purely non-linear with respect to optimization parameters. This figure can be very useful for engineers when they are designing artifacts to find out a design point passing their presumed criteria and to figure out how changing the design point would affect the performance of the artifact.

According to the results plotted in Fig. 11, we can roughly argue that there are two domains where  $L_c$  becomes minimum

$$\begin{aligned} Dom(L_{c_{min}})_1 &= \{(\theta, x_{slot}) \in \mathbb{R} | 25^\circ < \theta < 65^\circ, 0 < x_{slot} < 0.15\} \\ Dom(L_{c_{min}})_2 &= \{(\theta, x_{slot}) \in \mathbb{R} | 72.5^\circ < \theta < 85^\circ, 0.1 < x_{slot} < 0.4\} \end{aligned} \quad (21)$$

and there is one domain that  $C_l$  becomes maximum

$$Dom(C_{l_{max}}) = \{(\theta, x_{slot}) \in \mathbb{R} | 40^\circ < \theta < 85^\circ, 0.15 < x_{slot} < 0.4\} \quad (22)$$

Then, it is expected that the optimized points placed in the set stated hereunder:

$$\begin{aligned} (Dom(C_{l_{max}}) \cap Dom(L_{c_{min}})_1) \cup (Dom(C_{l_{max}}) \cap Dom(L_{c_{min}})_2) \\ = \{(\theta, x_{slot}) \in \mathbb{R} | 72.5^\circ < \theta < 85^\circ, 0.15 < x_{slot} < 0.4\} \end{aligned} \quad (23)$$

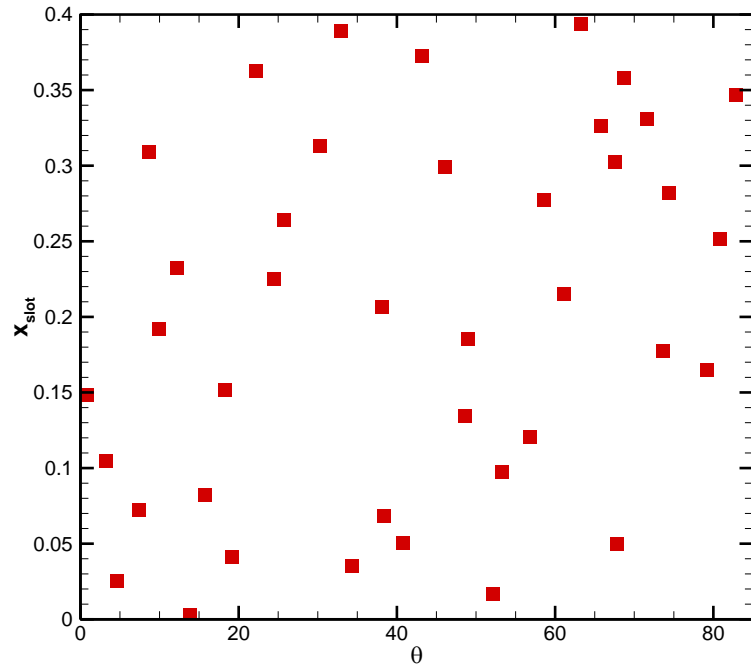
which is exactly corresponding with the domain that the optimizer seeks for the optimal points as depicted in the right upper part of Fig. 9(b). It is evident that the optimization process is suitably designed and works appropriately. Before presenting the optimal points, it is important to assess the accuracy of the surrogate model and its validity. For this aim, at different points along the midlines of the design space, the CFD results are compared with the data extracted from the surrogate model that are given in Table 1. The percentage of the error is defined as

$$\begin{aligned} Error(L_c) &= \frac{|L_{c_{CFD}} - L_{c_{surrogate}}|}{L_{c_{CFD}}} \times 100 \\ Error(C_l) &= \frac{|C_{l_{CFD}} - C_{l_{surrogate}}|}{|C_{l_{CFD}}|} \times 100 \end{aligned} \quad (24)$$

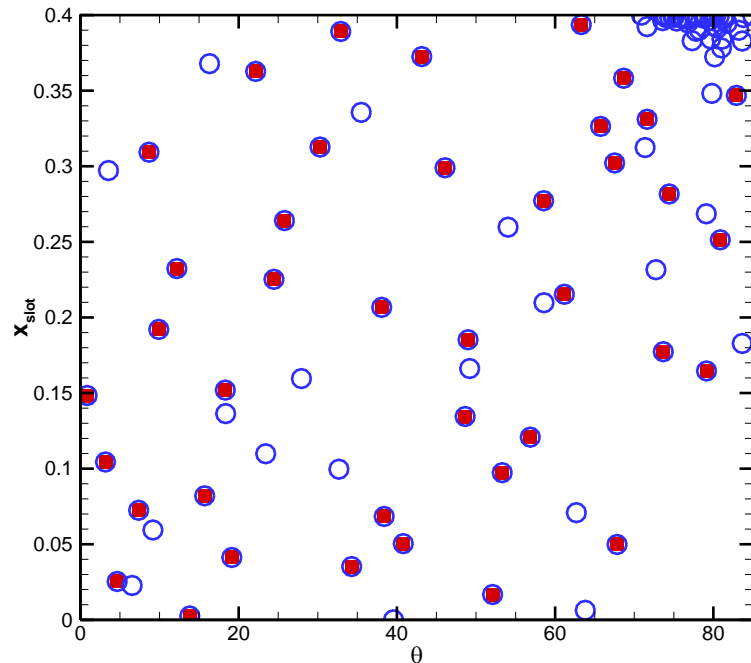
and it is seen that the maximum percentage of the error in predicting  $L_c$  is lower than 4.06 percent, while for  $C_l$  this error is lower than 2.24. These amount of errors are in an acceptable range and it

can be concluded that the surrogate model is trained properly and is reliable. In Figs. 12 and 13, the density and pressure contours for points used in Table 1 are plotted. From Fig. 12 and Table 1 it can be deduced that for  $\theta = 42.5^\circ$  and by pushing the slot from the middle chord to the leading-edge, the lift coefficient is desirably increased while the total length of cavity is unfavorably increased. However, from Fig. 13 and Table 1 it can be seen that for  $x_{slot} = 0.2$  and by increasing the slot angle, while  $L_c$  is always desirably decreasing,  $C_l$  is first decreasing and then increasing. In general, both of  $C_l(x_{slot}, \theta)$  and  $L_c(x_{slot}, \theta)$  are non-linear.

In Table 2, the output of the optimization process which is the Pareto front is given. While any point in the Pareto front is a candidate to be served as an optimal point, another criterion should be added to help the optimal point selection. This criterion is arbitrary. Here, we are seeking a point that shows the best performance in comparison with the average values of all points in the Pareto front. These average values are indicated by  $\bar{L}_c$  and  $\bar{C}_l$  and are presented in the last row. In other words, the optimal point would be a point with  $\max(\bar{L}_c - L_c)$  and  $\max(C_l - \bar{C}_l)$  which is obtained for  $(\theta, x_{slot}) = (80.461, 0.354)$ . In Fig. 14, generated grid for the slotted hydrofoil is shown, and similar to the original hydrofoil illustrated in Fig. 4 a finer grid resolution is utilized in comparison with the one far enough from the hydrofoil surface. The pressure contour with streamlines and the density contour is depicted in Fig. 15. It can be seen that by the slot the fluid with higher-pressure on the lower surface of the hydrofoil is transmitted to the suction side with lower-pressure resulting in shrinking the cavity pocket. In fact, the high-pressure fluid is injected to the suction side with lower-pressure and prevents the pressure becomes lower than the vapor pressure and subsequently results in not to happen cavitation. However, injecting a high-pressure fluid over the hydrofoil will decrease the lift coefficient. This phenomenon can be clearly seen in Fig. 16 that the pressure coefficient over the surface of the optimized slotted hydrofoil is compared with the original hydrofoil. In this way, we are able to favorably shrink the cavity pocket, but the lift coefficient will be disadvantageously decreased. Basically, imposing higher pressure over the upper surface of the hydrofoil will cause a downward force that means decreasing in the lift. The total length of the cavity that appeared on the suction side for the optimized slotted hydrofoil is  $L_c = 0.2006$ , while it is 0.482 for the original hydrofoil that shows an improvement. In the case of the lift coefficient, it equals 0.6098 for the optimized slotted hydrofoil while it is 0.688 for the original hydrofoil that shows a deterioration. These results indicate that with a penalty of about 11.4% in the lift coefficient, it is possible to decrease the cavity size by about 58.4%.

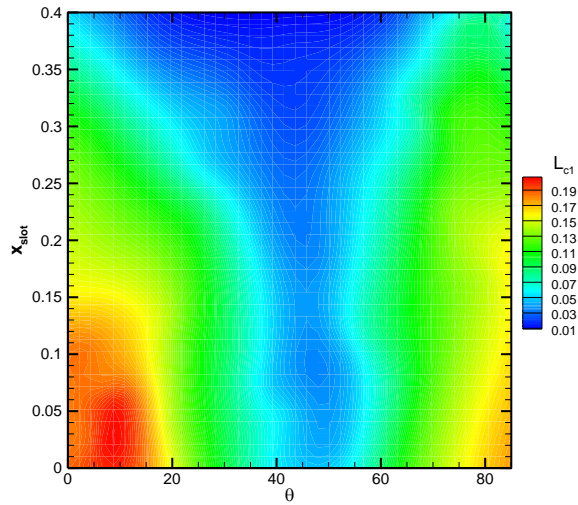


(a)

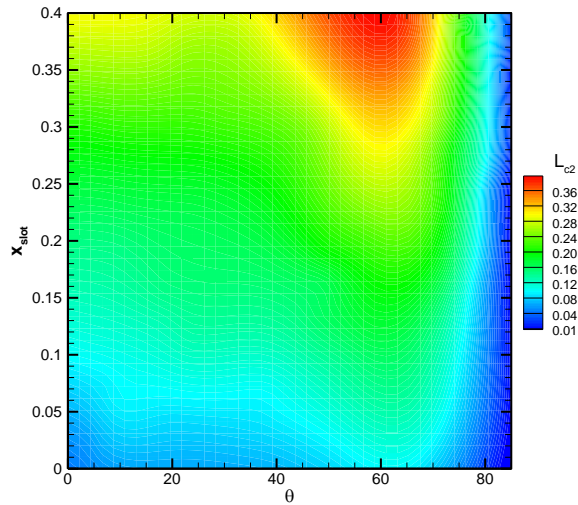


(b)

Fig. 9 a) Initial sampling using 40 points and b) final training samples.

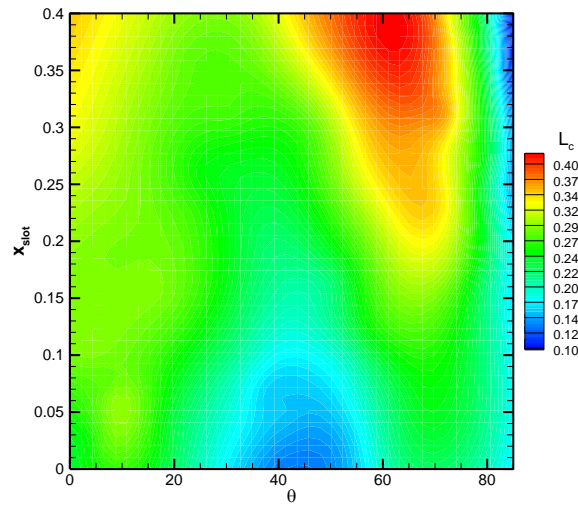


(a)

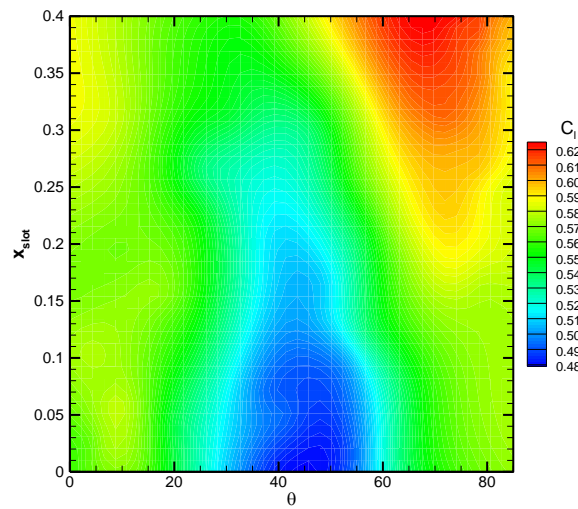


(b)

Fig. 10 Contours for a)  $L_{c1}$  and b)  $L_{c2}$  obtained using the fitting method.



(a)



(b)

Fig. 11 Contours for a)  $L_c$  and b)  $C_l$  obtained using the fitting method.

Table 1 Investigation of the accuracy of the surrogate model

$\theta$	$x_{slot}$	CFD		Surrogate model		Error (%)	
		$L_c$	$C_l$	$L_c$	$C_l$	$L_c$	$C_l$
$42.5^\circ$	0.00	0.118	0.476	0.123	0.484	4.778	1.591
$42.5^\circ$	0.20	0.231	0.519	0.222	0.514	3.723	0.966
$42.5^\circ$	0.40	0.323	0.564	0.339	0.577	4.978	2.244
$0.0^\circ$	0.20	0.284	0.574	0.297	0.575	4.532	0.068
$42.5^\circ$	0.20	0.231	0.519	0.222	0.514	3.723	0.966
$85.0^\circ$	0.20	0.157	0.584	0.162	0.586	2.852	0.286

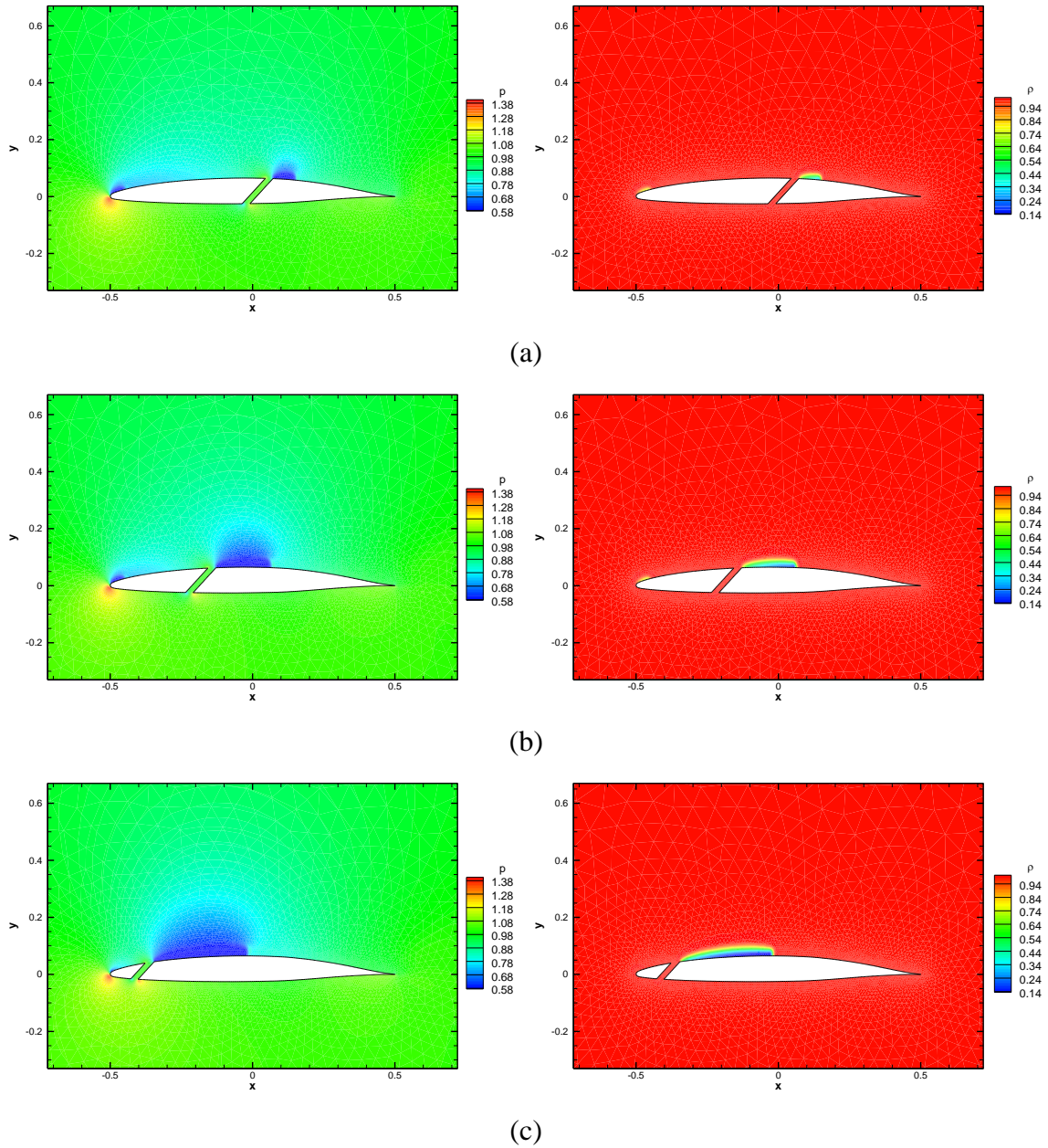


Fig. 12 The pressure (left column) and density (right column) contours for  $\theta = 42.5^\circ$  and a)  
 $x_{slot} = 0.0$ , b) 0.2, and c) 0.4

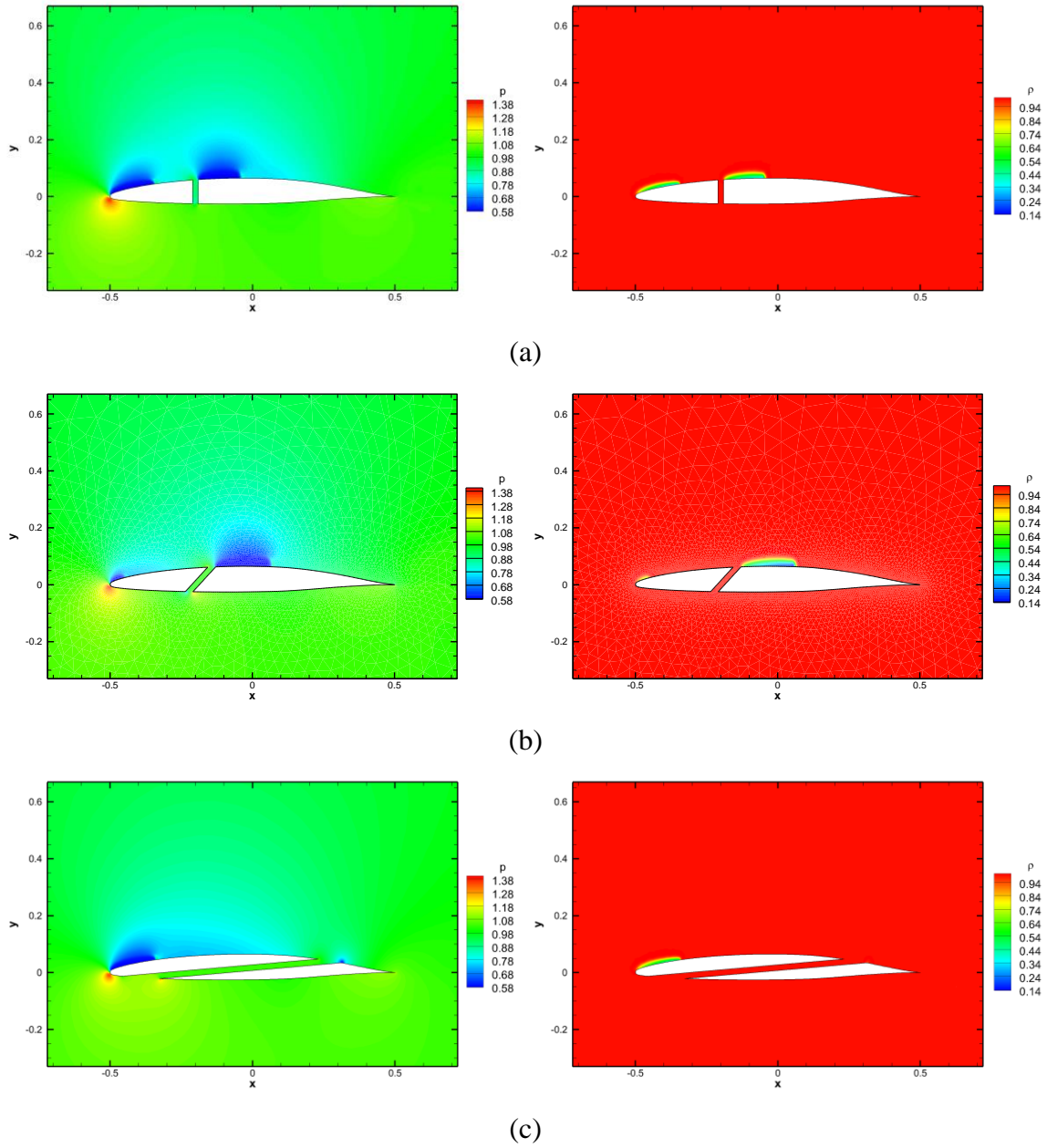


Fig. 13 The pressure (left column) and density (right column) contours for  $x_{slot} = 0.2$  and a)  
 $\theta = 0.0^\circ$ , b)  $42.5^\circ$ , and c)  $85.0^\circ$ .

Table 2 Pareto front points (GA output)

$\theta$	$x_{slot}$	$L_c$	$C_l$	$\bar{L}_c - L_c$	$C_l - \bar{C}_l$	
84.545	0.003	0.1293	0.5976	0.0814	-0.0119	
80.780	0.094	0.1945	0.6091	0.0162	-0.0005	
79.936	0.192	0.2107	0.6112	0.0001	0.0017	
78.943	0.138	0.2295	0.6132	-0.0187	0.0036	
75.576	0.146	0.2882	0.6169	-0.0775	0.0073	
80.461	0.354	0.2006	0.6098	0.0102	0.0003	Selected
79.473	0.284	0.2196	0.6123	-0.0089	0.0028	
76.866	0.339	0.2676	0.6164	-0.0569	0.0068	
82.397	0.111	0.1648	0.6046	0.0460	-0.0050	
78.373	0.198	0.2402	0.6143	-0.0295	0.0047	
77.263	0.247	0.2605	0.6158	-0.0497	0.0063	
82.786	0.003	0.1578	0.6033	0.0529	-0.0063	
82.999	0.047	0.1542	0.6027	0.0566	-0.0069	
83.464	0.202	0.1465	0.6014	0.0643	-0.0082	
78.811	0.302	0.2322	0.6136	-0.0215	0.0041	
76.170	0.073	0.2786	0.6165	-0.0679	0.0070	
84.996	0.001	0.1228	0.5961	0.0880	-0.0135	
75.117	0.400	0.2958	0.6173	-0.0850	0.0077	
		$\bar{L}_c = 0.2107$	$\bar{C}_l = 0.6096$			

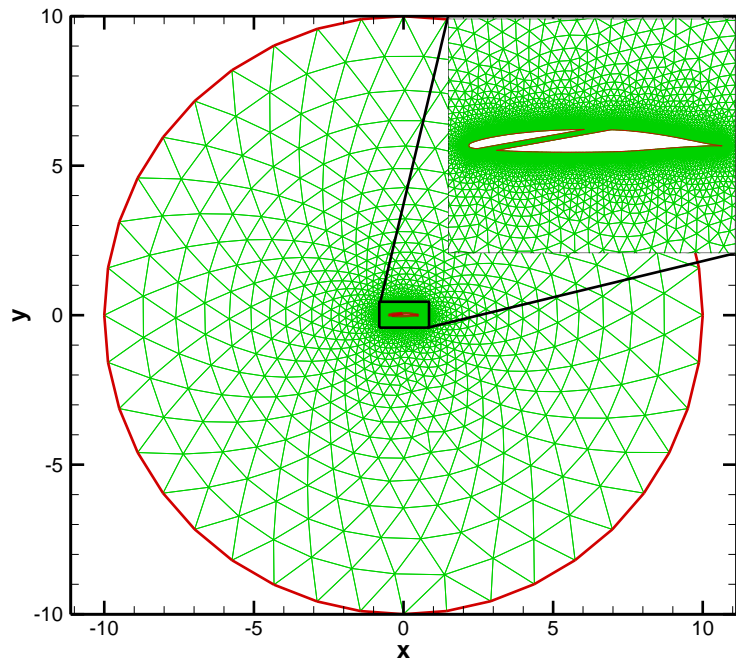
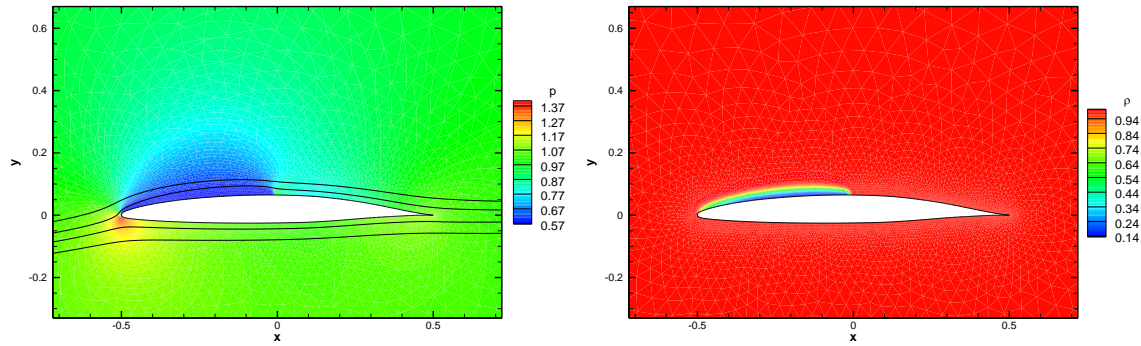
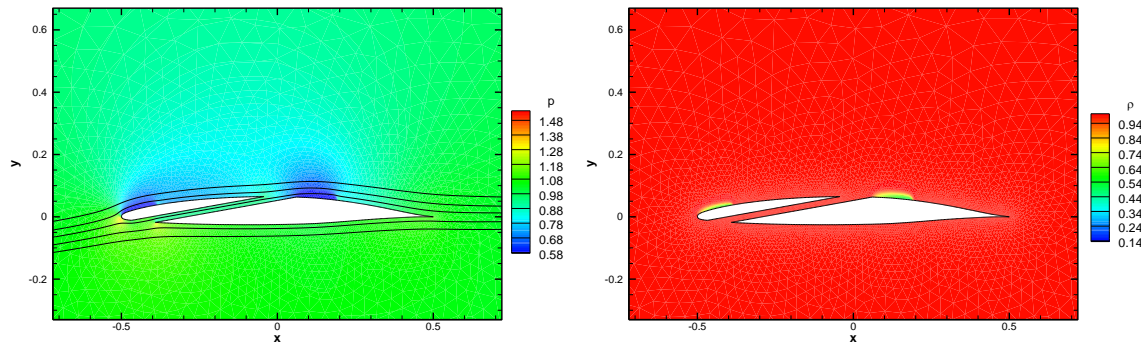


Fig. 14 Generated grid for the optimal slotted NACA 66 (MOD) hydrofoil.

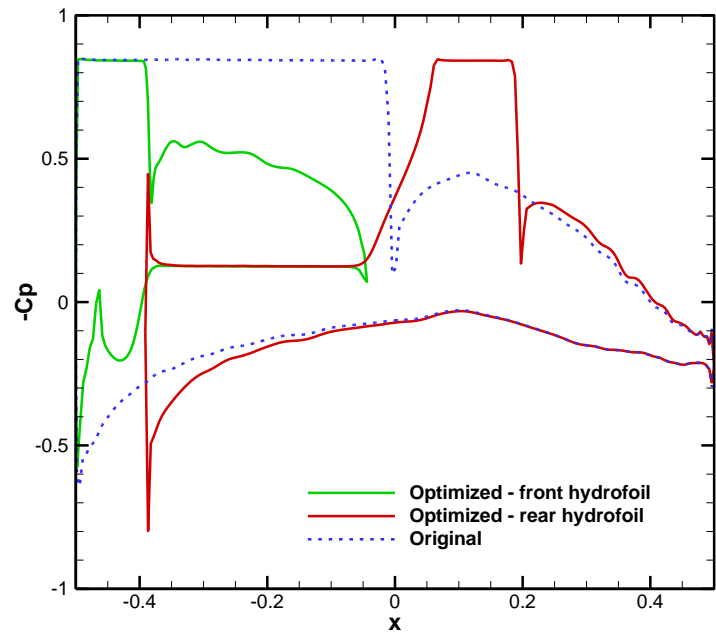


(a)

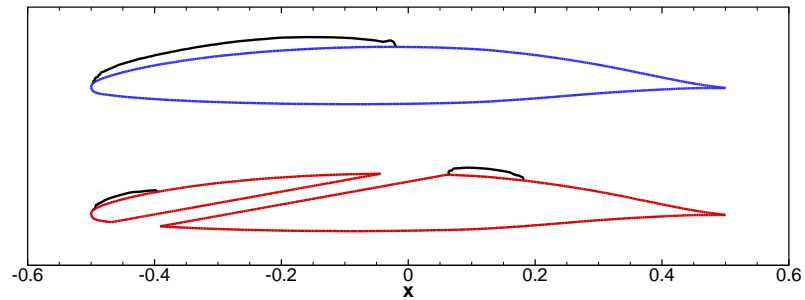


(b)

Fig. 15 The pressure (left column) and density (right column) contours for a) the original hydrofoil and for b) the optimized slotted hydrofoil.



(a)



(b)

Fig. 16 a) pressure coefficient distribution over the hydrofoil surfaces and b) their corresponding shape and the cavity pocket indicated by  $C_p = -\sigma$ .

## 6. Conclusion

In this paper, optimization is done to find out the slot location and the slot angle that result in maximizing the lift coefficient and minimizing the total length of the cavity. Through the optimization procedure, a computational fluid dynamic (CFD) solver is required to provide the lift coefficient and the total length of the cavity for the optimizer. For this aim, the Frink numerical method is used here to discretize the spatial terms in the preconditioned Euler equations based on the artificial compressibility method. The artificial dissipation terms are added to these equations for stability reasons and a sensor is used to retain the solution accuracy in smooth regions. Moreover, source terms that model the cavitation process are also added to the equations. The optimizer is constructed using a surrogated model based on the kriging metamodel and the genetic algorithm. Here, the Latin Hypercube algorithm is used to generate initial sample points. The outcome of the optimization process is an optimized slotted NACA 66 (MOD) hydrofoil satisfying the cost functions defined. Some conclusions and remarks regarding the present work are as follows:

- The comparison between results obtained by the CFD solver and available experimental results shows that the numerical method proposed here can be effectively used for simulating cavitating flows and can be considered as an alternative for the other cavitating flow solvers.
- For the original hydrofoil NACA 66 (MOD), one cavity pocket is formed on its suction side. However, in the slotted hydrofoil, two cavities will be emerged on the hydrofoil surface, namely, the leading-edge and mid-chord cavities. Smaller leading-edge cavity size will be found around  $\theta = 45^\circ$  and at high slot angles. In the case of the mid-chord cavity, higher slot angles should be used with a slot placed around the middle.
- From the results obtained it can be concluded that high slot angles and high slot locations desirably result in the small total length of the cavity  $L_c$  and high lift coefficient  $C_l$ .
- The surrogated mode is examined against CFD results which shows a good agreement, thus it can be reliably used in the genetic algorithm for optimizing purposes.
- Results obtained for the optimum design point selected from the Pareto front show that with a penalty of about 11.4% in the lift coefficient, it is possible to decrease the cavity size by about 58.4%.

- The contours for the lift coefficient, the total length of the cavity, the length of the leading-edge cavity, and the length of the mid-chord cavity obtained in this study can be used by engineers to figure out how deviation from the optimum point can affect the performance of their products.

## Acknowledgment

## References

- [1] E. Lauga, M. Brenner, H. Stone, C. Tropea, A. L. Yarin, and J. F. Foss, "Springer handbook of experimental fluid mechanics," ed: Springer Berlin, Heidelberg, 2007.
- [2] C. S. Pant, Y. Delorme, and S. Frankel, "Accuracy Assessment of RANS Predictions of Active Flow Control for Hydrofoil Cavitation," *Processes*, vol. 8, no. 6, 2020.
- [3] C.-S. Lee, B.-K. Ahn, J.-M. Han, and J.-H. Kim, "Propeller tip vortex cavitation control and induced noise suppression by water injection," *Journal of Marine Science and Technology*, vol. 23, no. 3, pp. 453-463, 2018/09/01 2018.
- [4] M. G. De Giorgi, A. Ficarella, and D. Fontanarosa, "Active Control of Unsteady Cavitating Flows in Turbomachinery," 2019. Available: <https://doi.org/10.1115/GT2019-92041>
- [5] W. Wang, Q. Zhang, T. Tang, S. Lu, Q. Yi, and X. Wang, "Numerical study of the impact of water injection holes arrangement on cavitation flow control," *Science Progress*, vol. 103, no. 1, p. 0036850419877742, 2020.
- [6] P. Akbarzadeh and E. Akbarzadeh, "Hydrodynamic characteristics of blowing and suction on sheet-cavitating flows around hydrofoils," *Ocean Engineering*, vol. 114, no. C, pp. 25-36, 2016.
- [7] B. Che and D. Wu, "Study on Vortex Generators for Control of Attached Cavitation," 2017. Available: <https://doi.org/10.1115/FEDSM2017-69405>
- [8] B. Che, N. Chu, L. Cao, S. J. Schmidt, D. Likhachev, and D. Wu, "Control effect of micro vortex generators on attached cavitation instability," *Physics of Fluids*, vol. 31, no. 6, p. 064102, 2019.
- [9] Q. Wei, H.-x. Chen, and R. Zhang, "Numerical research on the performances of slot hydrofoil," *Journal of Hydrodynamics, Ser. B*, vol. 27, no. 1, pp. 105-111, 2015/02/01 / 2015.
- [10] Z. Li, Z. Qian, and B. Ji, "Transient cavitating flow structure and acoustic analysis of a hydrofoil with whalelike wavy leading edge," *Applied Mathematical Modelling*, vol. 85, pp. 60-88, 2020/09/01/ 2020.
- [11] T. Capurso, M. Lorusso, S. M. Camporeale, B. Fortunato, and M. Torresi, "Implementation of a passive control system for limiting cavitation around hydrofoils," vol. 240, p. 032025: IOP Publishing.

- [12] T. Capurso, G. Menchise, G. Caramia, S. M. Camporeale, B. Fortunato, and M. Torresi, "Investigation of a passive control system for limiting cavitation inside turbomachinery under different operating conditions," *Energy Procedia*, vol. 148, pp. 416-423, 2018/08/01/ 2018.
- [13] F. R. cones and R. Liem, "Numerical investigation of cavitation performance of slotted hydrofoil for amphibious aircraft applications," 2018.
- [14] F. R. Conesa and R. P. Liem, "Slotted hydrofoil design optimization to minimize cavitation in amphibious aircraft application: A numerical simulation approach," *Advances in aircraft and spacecraft science*, vol. 7, no. 4, pp. 309-333, 2020.
- [15] Z. Ni, M. Dhanak, and T.-c. Su, "Performance of a slotted hydrofoil operating close to a free surface over a range of angles of attack," *Ocean Engineering*, vol. 188, p. 106296, 2019/09/15/ 2019.
- [16] E. Kadivar, O. e. Moctar, and K. Javadi, "Stabilization of cloud cavitation instabilities using Cylindrical Cavitating-bubble Generators (CCGs)," *International Journal of Multiphase Flow*, vol. 115, pp. 108-125, 2019/06/01/ 2019.
- [17] E. L. Amromin, "Design approach for cavitation tolerant hydrofoils and blades," *Journal of Fluids and Structures*, vol. 45, pp. 96-106, 2014/02/01/ 2014.
- [18] Q. Chen, Y. Liu, Q. Wu, Y. Wang, T. Liu, and G. Wang, "Global cavitation patterns and corresponding hydrodynamics of the hydrofoil with leading edge roughness," *Acta Mechanica Sinica*, 2020/10/01 2020.
- [19] A. Ducoin, Y. L. Young, and J.-F. o. Sigrist, "Hydroelastic Responses of a Flexible Hydrofoil in Turbulent, Cavitating Flow," 2010. Available: <https://doi.org/10.1115/FEDSM-ICNMM2010-30310>
- [20] A. Kubota, H. Kato, and H. Yamaguchi, "A new modelling of cavitating flows: a numerical study of unsteady cavitation on a hydrofoil section," *Journal of Fluid Mechanics*, vol. 240, pp. 59-96, 1992.
- [21] J. H. Seo, Y. J. Moon, and B. R. Shin, "Prediction of cavitating flow noise by direct numerical simulation," *Journal of Computational Physics*, vol. 227, no. 13, pp. 6511-6531, 2008/06/20/ 2008.
- [22] J. G. Zheng, B. C. Khoo, and Z. M. Hu, "Simulation of Wave-Flow-Cavitation Interaction Using a Compressible Homogenous Flow Method," *Communications in Computational Physics*, vol. 14, no. 2, pp. 328-354, 2013.
- [23] Y. Chen, X. Chen, Z. Gong, J. Li, and C. Lu, "Numerical investigation on the dynamic behavior of sheet/cloud cavitation regimes around hydrofoil," *Applied Mathematical Modelling*, vol. 40, no. 11, pp. 5835-5857, 2016/06/01/ 2016.
- [24] M. Dumbser, U. Iben, and C.-D. Munz, "Efficient implementation of high order unstructured WENO schemes for cavitating flows," *Computers & Fluids*, vol. 86, pp. 141-168, 2013/11/05/ 2013.
- [25] F. Örley, V. Pasquariello, S. Hickel, and N. A. Adams, "Cut-element based immersed boundary method for moving geometries in compressible liquid flows with cavitation," *Journal of Computational Physics*, vol. 283, pp. 1-22, 2015/02/15/ 2015.
- [26] T. Uchiyama, "Numerical simulation of cavitating flow using the upstream finite element method," *Applied Mathematical Modelling*, vol. 22, no. 4, pp. 235-250, 1998/04/01/ 1998.
- [27] M. Hajihassanpour and K. Hejranfar, "A high-order nodal discontinuous Galerkin method to solve preconditioned multiphase Euler/Navier-Stokes equations for inviscid/viscous cavitating flows," *International Journal for Numerical Methods in Fluids*, <https://doi.org/10.1002/fld.4792> vol. 92, no. 5, pp. 478-508, 2020/05/01 2020.
- [28] K. Hejranfar and M. Hajihassanpour, "A high-order nodal discontinuous Galerkin method for solution of compressible non-cavitating and cavitating flows," *Computers & Fluids*, vol. 156, pp. 175-199, 2017/10/12/ 2017.
- [29] N. Frink, "Recent progress toward a three-dimensional unstructured Navier-Stokes flow solver," in *32nd Aerospace Sciences Meeting and Exhibit*(Aerospace Sciences Meetings: American Institute of Aeronautics and Astronautics, 1994.

- [30] A. Jameson, W. Schmidt, and E. L. I. Turkel, "Numerical solution of the Euler equations by finite volume methods using Runge Kutta time stepping schemes," in *14th Fluid and Plasma Dynamics Conference*(Fluid Dynamics and Co-located Conferences: American Institute of Aeronautics and Astronautics, 1981.
- [31] G. G. Wang and S. Shan, "Review of Metamodeling Techniques in Support of Engineering Design Optimization," *Journal of Mechanical Design*, vol. 129, no. 4, pp. 370-380, 2006.
- [32] J. P. C. Kleijnen, "Kriging metamodeling in simulation: A review," *European Journal of Operational Research*, vol. 192, no. 3, pp. 707-716, 2009/02/01/ 2009.
- [33] A. Serani *et al.*, "Adaptive multi-fidelity sampling for CFD-based optimisation via radial basis function metamodels," *International Journal of Computational Fluid Dynamics*, vol. 33, no. 6-7, pp. 237-255, 2019/08/09 2019.
- [34] J. Qian, J. Yi, Y. Cheng, J. Liu, and Q. Zhou, "A sequential constraints updating approach for Kriging surrogate model-assisted engineering optimization design problem," *Engineering with Computers*, vol. 36, no. 3, pp. 993-1009, 2020/07/01 2020.
- [35] G. Wahba, *Spline models for observational data*. SIAM, 1990.
- [36] P. M. Zadeh, V. V. Toropov, and A. S. Wood, "Metamodel-based collaborative optimization framework," *Structural and Multidisciplinary Optimization*, vol. 38, no. 2, pp. 103-115, 2009/04/01 2009.
- [37] G. Li, V. Aute, and S. Azarm, "An accumulative error based adaptive design of experiments for offline metamodeling," *Structural and Multidisciplinary Optimization*, vol. 40, no. 1, p. 137, 2009/06/10 2009.
- [38] D. Simon, *Evolutionary optimization algorithms*. John Wiley & Sons, 2013.
- [39] A. Gogna and A. Tayal, "Metaheuristics: review and application," *Journal of Experimental & Theoretical Artificial Intelligence*, vol. 25, no. 4, pp. 503-526, 2013/12/01 2013.
- [40] M. Mitchell, "An introduction to genetic algorithms mit press," *Cambridge, Massachusetts. London, England*, vol. 1996, 1996.
- [41] M. Hajihassanpour and K. Hejranfar, "An implicit dual-time stepping high-order nodal discontinuous Galerkin method for solving incompressible flows on triangle elements," *Mathematics and Computers in Simulation*, vol. 168, pp. 173-214, 2020/02/01/ 2020.
- [42] C. L. Merkle, "Computational modelling of the dynamics of sheet cavitation."
- [43] R. F. Kunz *et al.*, "A preconditioned Navier–Stokes method for two-phase flows with application to cavitation prediction," *Computers & Fluids*, vol. 29, no. 8, pp. 849-875, 2000/08/31/ 2000.
- [44] I. Senocak and W. Shyy, "Interfacial dynamics-based modelling of turbulent cavitating flows, Part-1: Model development and steady-state computations," *International Journal for Numerical Methods in Fluids*, <https://doi.org/10.1002/fld.692> vol. 44, no. 9, pp. 975-995, 2004/03/30 2004.
- [45] A. K. Singhal, "Multi-dimensional simulation of cavitating flows using a PDF model of phase change."
- [46] P. J. Zwart, A. G. Gerber, and T. Belamri, "A two-phase flow model for predicting cavitation dynamics," vol. 152.
- [47] K. Hejranfar, E. Ezzatneshan, and K. Fattah-Hesari, "A comparative study of two cavitation modeling strategies for simulation of inviscid cavitating flows," *Ocean Engineering*, vol. 108, pp. 257-275, 2015/11/01/ 2015.
- [48] Y. Shen and P. E. Dimotakis, "The influence of surface cavitation on hydrodynamic forces," in *22nd American Towing Tank Conference*, St. John's, Newfoundland, Canada, 1989.